Theoretical design on the characteristics of a hexagon quasi- zero stiffness vibration isolator

Yingli Li (liyingli@csu.edu.cn)
Central South University https://orcid.org/0000-0002-5843-2848
Wenxi Zhou
Central South University

Research Article

Keywords: Quasi-zero stiffness, Low frequency, Vibration isolation, Tunable load capacity, Nonlinear properties.

Posted Date: March 23rd, 2022

DOI: https://doi.org/10.21203/rs.3.rs-1458175/v1

Theoretical design on the characteristics of a hexagon quasi-zero stiffness vibration isolator

Yingli Li[1,2,4*], Wenxi Zhou[1,3]

[1] *Key Laboratory of Traffic Safety on Track (Central South University), Ministry of Education, School of Traffic and Transportation Engineering, Central South University, Changsha, China 410075*

[2] *Joint International Research Laboratory of Key Technology for Rail Traffic Safety, Central South University, Changsha, China*

[3] *National & Local Joint Engineering Research Center of Safety Technology for Rail Vehicle, Central South University, Changsha, China*

[4] *State Key Laboratory of High Performance Complex Manufacturing, Central South University, Changsha, China*

ABSTRACT

A novel hexagon quasi-zero stiffness (QZS) platform using link-spring mechanism is proposed with load adjustable to seek for low-frequency vibration isolation. First, the key static characteristics, such as the elastic potential energy, restoring force and effective stiffness are obtained by mechanical modeling for different configurations of the platform. It indicates that the proposed structure could achieve dynamic zero stiffness for different designed loading capacity, even a full band vibration isolation. Then, the nonlinear properties of inertia, stiffness and damping are systematically studied and it is proven to be beneficial for dynamic stabilization and vibration isolation. An analytical expression for the effective stiffness is derived to obtain parameter condition for QZS characteristic. Finally, the displacement transmissibility of the structure is solved by the harmonic balance method. The results demonstrate that the hexagon QZS vibration isolator has low and tunable frequency for vibration isolation and outperforms the linear isolators. Comparing to the classical QZS vibration isolator, the proposed one has a wider zero stiffness plateau and the starting frequency of vibration isolation can be as low as 1/4 that of the classical one. Consequently, the hexagon QZS isolator should be a feasible design for vibration isolation in ultralow frequency range.

[*] Corresponding author:

Tel.: +86139 7487 2828; Email address: liyingli@csu.edu.cn

Keyword: Quasi-zero stiffness; Low frequency; Vibration isolation; Tunable load capacity; Nonlinear properties.

1. Introduction

The unwanted vibration generated in the engineering practice is unavoidable and is considered as a negative factor [1, 2], which may cause structural fatigue damage, produce offensive and reduce the life of the equipment. Therefore, an excellent vibration isolation system need to be applied to control the vibration in a reasonably range, such as vehicle suspension systems [3], on-orbit spacecraft [4] or high-precision machinery [5] and so on. According to the vibration isolation theory, it is known that the linear vibration isolation system only takes effect when the external excitation frequency exceeds $\sqrt{2}$ times the natural frequency [6, 7]. This limits the failure of traditional isolators in attenuation vibration under low frequency excitation. Another way is decreasing the stiffness of the system to improve the performance of vibration isolators for a low-frequency range, which will lead to large deformation of the mechanism and result in instability. Hence, an ideal isolator is supposed to provide sufficient static stiffness to ensure the stability of the system while possess a low dynamic stiffness around the equilibrium position to obtain a lower natural frequency [8, 9]. This high-static-low-dynamic stiffness (HSLDS) characteristic has beneficial effects for vibration control and utilization due to its geometric stiffness nonlinearity.

To overcome the shortcomings in linear systems and achieve the HSLDS characteristics, many literatures have explored nonlinear vibration isolation methods to develop excellent vibration isolation performance in low-frequency range. One of the most popular topics is the quasi-zero stiffness (QZS) [10–13]. The realization of the QZS is to introduce a negative stiffness structure into a positive stiffness structure system. Negative stiffness mechanisms can be implemented with different structures or media with the geometric and stiffness parameters reasonably optimized to achieve QZS characteristics. The typical QZS vibration isolator proposed by Carrella was established by combining vertical spring with two oblique springs in parallel [14, 15]. Links [16] and bending beams [17] can also be introduced as negative stiffness mechanisms instead of oblique springs. In addition, Xu *et al* have developed several negative stiffness implementation methods, including cam sliders [18, 19], magnets [20], etc. The force transmissibility for different parameters has been deduced based on the harmonic balance method, and it was verified by experiments that the QZS vibration isolators can outperform the traditional linear vibration isolator, especially in low frequency. Based on that, Zhou has expanded these QZS structures to realize multi-directional vibration isolation, such as the six-degree-of-freedom platform [21], the bidirectional deep-subwavelength resonator [22]. At the same time, introducing the

electromagnetic mechanisms [23] and bi-stable control structures [24] to the QZS isolators can adjust the range of stiffness [25] or be designed as semi-active systems [26]. The isolators attached additional magnetic field equipment are restricted in miniature and lightweight devices due to its complicated structure. Hence, some researchers have concentrated on the X-shaped [27, 28], K-shaped [29, 30] and torsional vibration [31] isolators consisting of links and springs to realize the QZS systems.

In recently years, nonlinear vibration isolation methods have been developed by taking the advantages of the geometric nonlinearity incurred by links. Jing *et al* [32–35] have proposed a series of X-shaped structures for stability effect and excellent isolation with experimental verification. A bio-inspired anti-vibration structure was designed for vibration protection to operator when operating hand-held jackhammers in construction [33]. A systematic investigation on the properties of bio-inspired vertically asymmetric X-shape structure was carried out to explore the advantage of nonlinear characteristics in practical engineering [34]. A novel and compact X-shaped vibration isolation mount was analyzed [35]. A special oblique and tunable spring mechanism was designed in the novel mount to be adjustable to different load capacity, which had a high vibration isolation performance with a wider QZS range. In addition, Sun has proposed a novel multi-layer structure bio-inspired by the role of an avian neck [36], the unit cell of the structure performed like a diamond. It has been seen that the proposed structure can solve the bottleneck techniques in nonlinear vibration isolation design and has potential applications in fields of sensors in satellites, mechanical arms, etc. Yan designed a large stroke QZS vibration isolator using three-link mechanisms [37]. This novel design provided a feasible method for large amplitude and low frequency vibration isolation. For traditional QZS isolators, the zero-stiffness can only be realized around the equilibrium point, the effective stiffness of the QZS system increases rapidly once a large displacement occurs from the equilibrium. The QZS cannot work effectively when the vibration amplitudes excess QZS region, which cannot adapt for the various and time-varying vibration amplitude and frequency in practical applications. Hence, how to broaden the range of QZS and adjust the load capacity become a focus.

In this study, a novel design of QZS vibration isolator is proposed with a hexagon shape containing two two-link mechanisms. Linear springs are installed in different positions to achieve positive or negative stiffness. The QZS characteristics can be flexibly adjusted by structural parameters and appropriate stiffness ratio based on the specific analytical expressions, even a full range of QZS can be realized under a certain configuration. The dynamical model is established in Lagrange equation and solved by harmonic balance method under the periodic excitation. The vibration isolation

performance of the proposed system could be intuitively described by the displacement transmissibility.

The rest of the paper is organized as follows. In Section **2**, a hexagon structure consisting of two two-link mechanisms is firstly proposed and its static stiffness is analyzed under different structural parameters. Based on the geometrical nonlinearity, the load capacity and effective work range can be optimized by setting suitable springs and an initial angle of the structure. In Section **3**, the nonlinearity of the inertia, stiffness and damping are analyzed with respect to different parameters under dynamic condition. In Section **4**, the displacement transmissibility is solved with different parameters and the vibration isolation performances are compared with the classical QZS isolator. Finally, conclusions are drawn in Section **5**.

2. Static modelling of the system

2.1 Mathematica modeling

The vibration isolator considered in this work is illustrated in **Fig. 1**a. It consists of a symmetric hexagon structure in the middle and two vertical springs on both sides. The symmetric hexagon structure consists of four lightweight links with a horizontal spring connected to two vertices, and mass of the joints on the vertices is set as m. The ends of the links are fixedly connected to the base and the tops are connected to the bearing platform. Two linear springs in vertical are distributed on both sides of the links and limited by two guiding mandrels. The bearing platform is only allowed to move in vertical direction. In additional, the gap distance between the vertical spring and the platform can be arbitrarily adjusted by a telescopic mechanism to change the load capacity and stiffness of the structure.

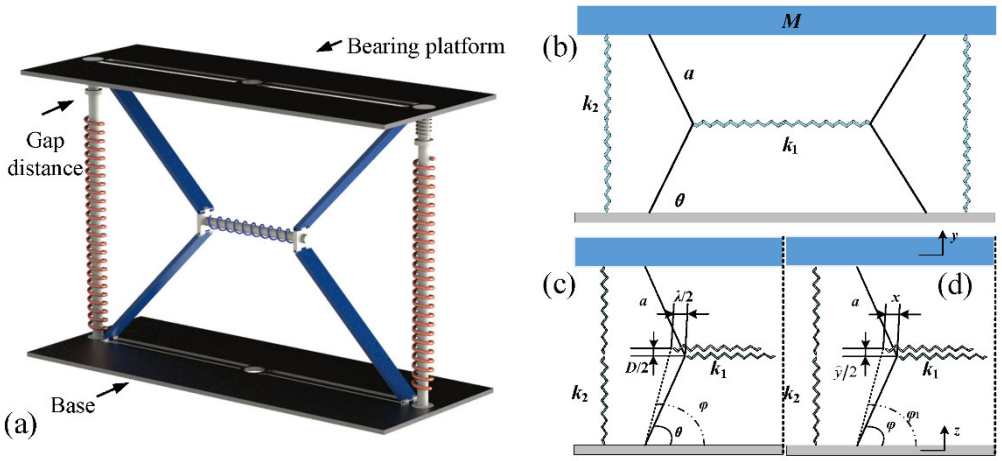

Fig. 1 A hexagon QZS vibration isolator with lightweight links and linear springs: **a** Physical model; **b** Schematic diagram; **c** Deformation of motion

For convenience in discussion, the proposed structure is simplified in **Fig. 1** with clear specification of structural parameters. The length of the links is a. The initial angle between the links and the horizontal line is θ without any load. According to **Fig. 1** , as the mass M applied on the bearing platform with a deformation D, the deformation of the horizontal elastic component is λ, and the angle θ becomes φ . Then the geometrical relation between D and λ is given as

$$\lambda = 2a\cos\theta - 2\sqrt{a^2 - \left(a\sin\theta + \frac{D}{2}\right)^2} \tag{1}$$

When the gap distance is zero, the deformation of each vertical spring can be expressed as D. The stiffness of the horizontal and vertical springs are k_{h} and k_{v}, respectively. Then, the elastic potential energy of the proposed structure with deformation D is defined as U, written as

$$U = \frac{1}{2}k_h\lambda^2 + 2\times\frac{1}{2}k_v D^2 \tag{2}$$

Fig. 2a shows the potential energy curves as a function of the displacement D for different initial angle θ. The displacement D of the bearing platform should be in the range [-2asinθ, 2a-2asinθ]. The potential energy curves are asymmetrical when the platform is stretched or compressed, and it changes more slowly around the equilibrium under a smaller angle. Vibration occurs around the equilibrium where the potential energy is smallest. According to the relation between the potential energy and restoring force, the latter can be derived as

$$F = \frac{\delta U}{\delta D} \tag{3}$$

Fig. 2b shows the relation between the restoring force F and the displacement D. The platform loses its load capacity for upward motion while has an adequate support force for downward, and it increases as the platform moves down. When the initial angle increases, the restoring force increases more obviously, and the move range becomes larger. The variation of restoring force performs nonlinear strengthening properties for upward motion and softening properties for downward motion. Hence, the hexagon QZS platform can be applied to large motion excitations induced by ultralow-frequency excitations.

2.2 Stiffness analysis

According to the nonlinearity embodied in restoring force, stiffness properties can be further analyzed, which can be defined as

$$K=\frac{\delta^2 U}{\delta D^2} \tag{4}$$

As shown in **Fig. 2**c, the stiffness curve has similar performance with that in restoring force in **Fig. 2**b. It has large values and increases dramatically when the platform moves up while it tends to be gentle for downward motion.

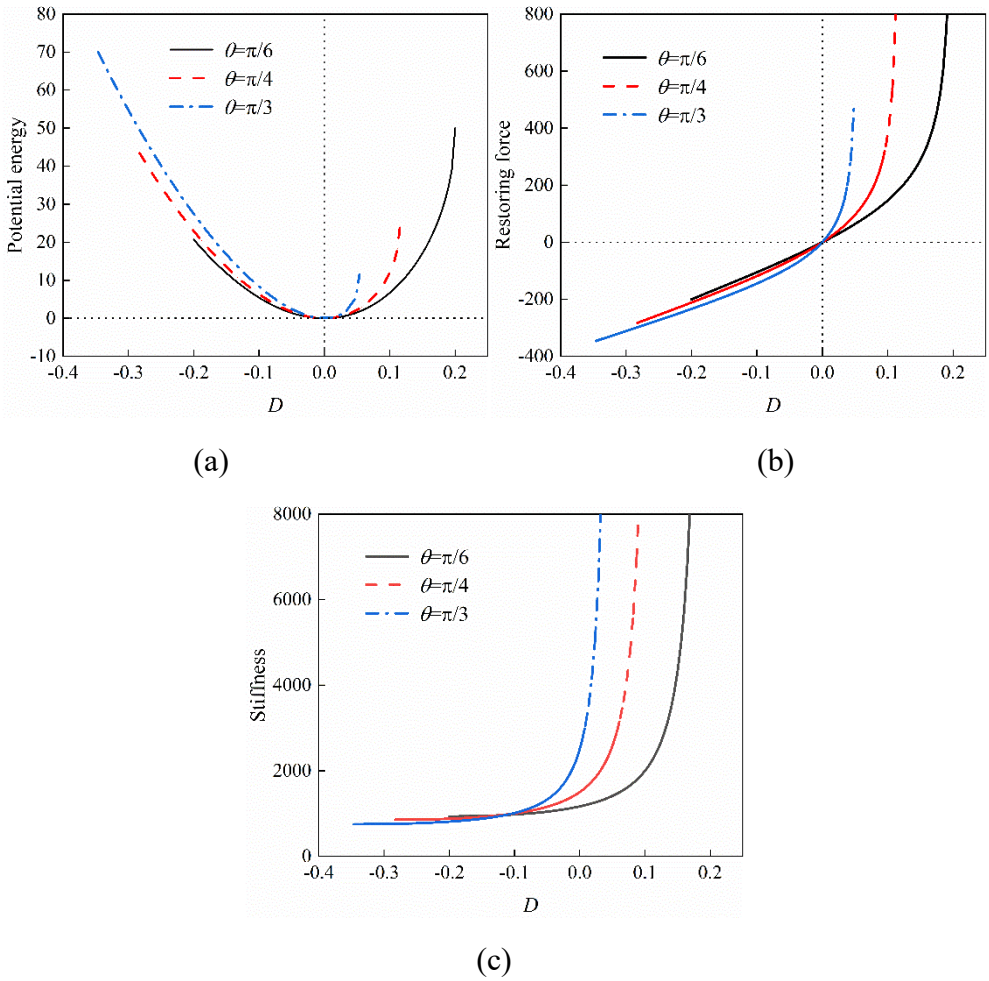

Fig. 2 a Potential energy, **b** restoring force, and **c** stiffness curves for different initial angles

The QZS characteristic of the system can be achieved by adjusting stiffness of the horizontal and vertical springs. Here, the stiffness k_v is fixed as 500 N/m and k_h changes. As shown in **Fig. 3**, the values of stiffness are quasi-zero under some certain values of k_v for different initial angles. Once the stiffness k_v increases or decreases, it performs positive and negative stiffness characteristics. Hence, the vertical springs provide positive stiffness and the horizontal spring provides nonlinear stiffness with positive or negative coefficients, respectively. When the initial angle θ increases, the effective range around QZS becomes wider, and the required stiffness k_v also increases.

Based on that, a limit configuration with the initial angle $\theta = \pi/2$ is presented to realize a wide QZS range, as shown in **Fig. 4**a. In this case, the deformation of

horizontal spring λ in Eq. (1) can be expressed as

$$\lambda' = -2\sqrt{a^2 - \left(a + \frac{D}{2}\right)^2} \tag{5}$$

Under static equilibrium, the input energy W_{input} caused by the load mass M can be expressed as

$$W_{\text{input}} = MgD + 2mg \times \frac{D}{2} \tag{6}$$

where m is the mass attached on the joints.

To ensure that the state of the platform can be stable during the downward motion, the gravitational energy W_{input} should be completely converted to the elastic potential energy of the system. The latter can be derived as

$$W_{\text{potential}} = \frac{1}{2}k_v\lambda'^2 + 2 \times \frac{1}{2}k_h D^2 \tag{7}$$

Two relations can be obtained when Equating Eq. (6) and (7), they are 1) $k_h = 2k_v$, and 2) $k_h = (M+m)g/2a$. These two requirements ensure that the platform can maintain equilibrium at any displacement D for the downward motion. In other words, the platform has a constant zero effective stiffness during the entire displacement range. When the platform moves down, the input energy W_{input} will be stored in the springs while it will be released to the load when moving up, two types of energy will always be equal. This phenomenon is similar with the full-band mechanical metamaterials mentioned in **work** [38], which is called an "energy circulation."

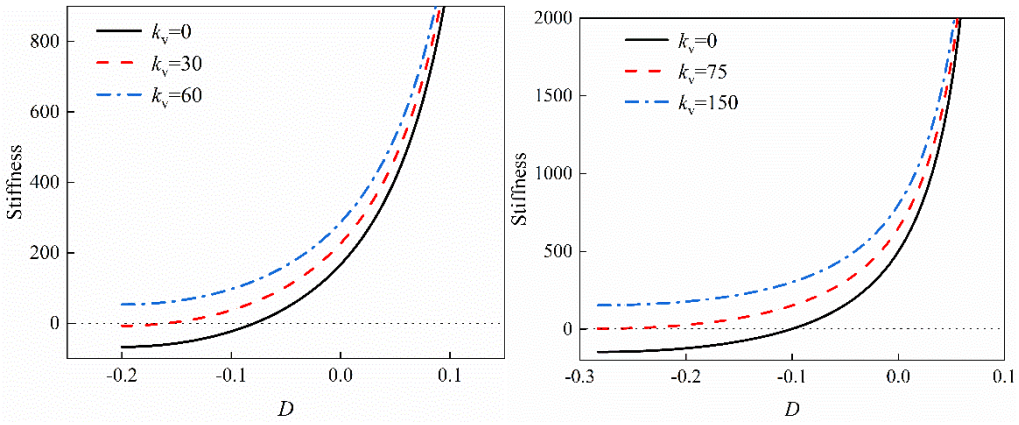

(a) (b)

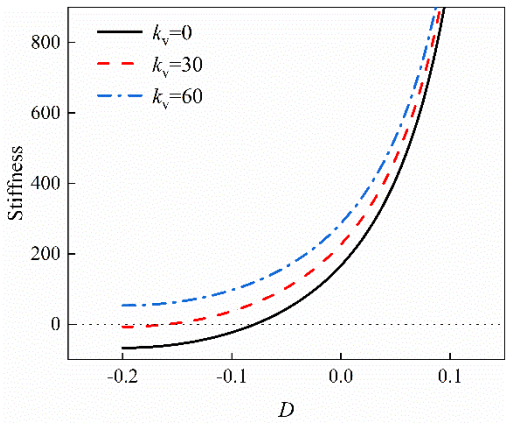

(c)

Fig. 3 Equivalent stiffness function K with different stiffness k_v for **a** θ =π/6, **b** θ =π/4, and **c** θ =π/3

Fig. 4b shows the potential energy curves for different vertical stiffness with the horizontal stiffness k_h=500 N/m. It is observed that the potential energy E becomes a linear function of displacement D when the stiffness ratio satisfies the requirement 1). Otherwise, the curve returns to weak nonlinearity. The restoring force becomes linear no matter how the stiffness ratio changes. Particularly, the restoring force maintains -200 N when the stiffness k_v=250 N/m in **Fig. 4**c, which reflects that the zero-stiffness platform with the entire displacement range can be only realized under a fixed load, refers to the requirement 2). The zero-stiffness characteristic is shown in **Fig. 4**d, which is a critical line for the positive or negative effective stiffness of the system as the vertical stiffness changes.

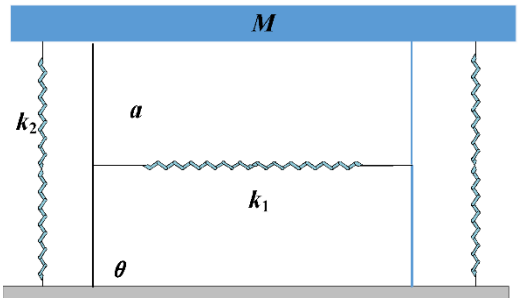

(a)

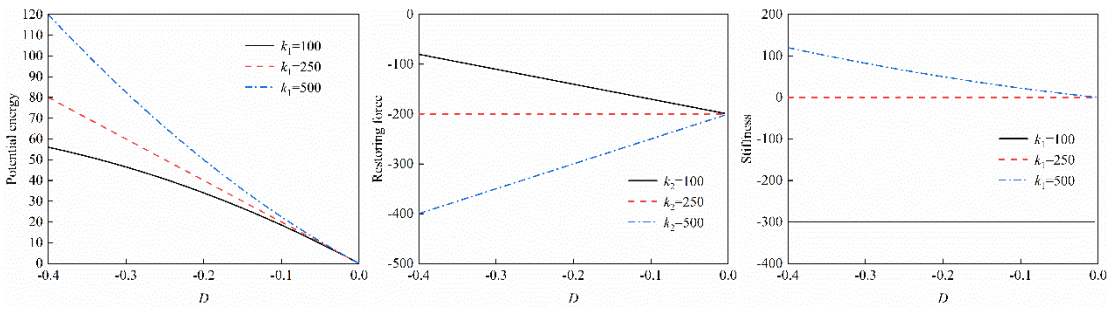

(b) (c) (d)

Fig. 4 a Schematic diagram of the limit configuration when $\theta = \pi/2$; **b** potential energy, **c** restoring force, and **d** stiffness curves with displacement D for different vertical stiffness k_v

In addition to changing the initial angle, the QZS characteristic can be also obtained by adjusting the gap distance d_g between the bearing platform and the vertical springs. The vertical springs are supposed to start work at the positions when the platform is compressed at 0.05, 0.1, 0.15 in **Fig. 5**. It is observed in **Fig. 5**a-d that the effective stiffness is gradually approaching zero when the platform is compressed around 0.25, although the gap distance is different. The restoring force under different gap distances is shown in **Fig. 5**e, which decreases as the gap distance increases. Hence, the load capacity can be conveniently adjusted by changing the gap distance with ensuring the QZS characteristic still exists in a large displacement range.

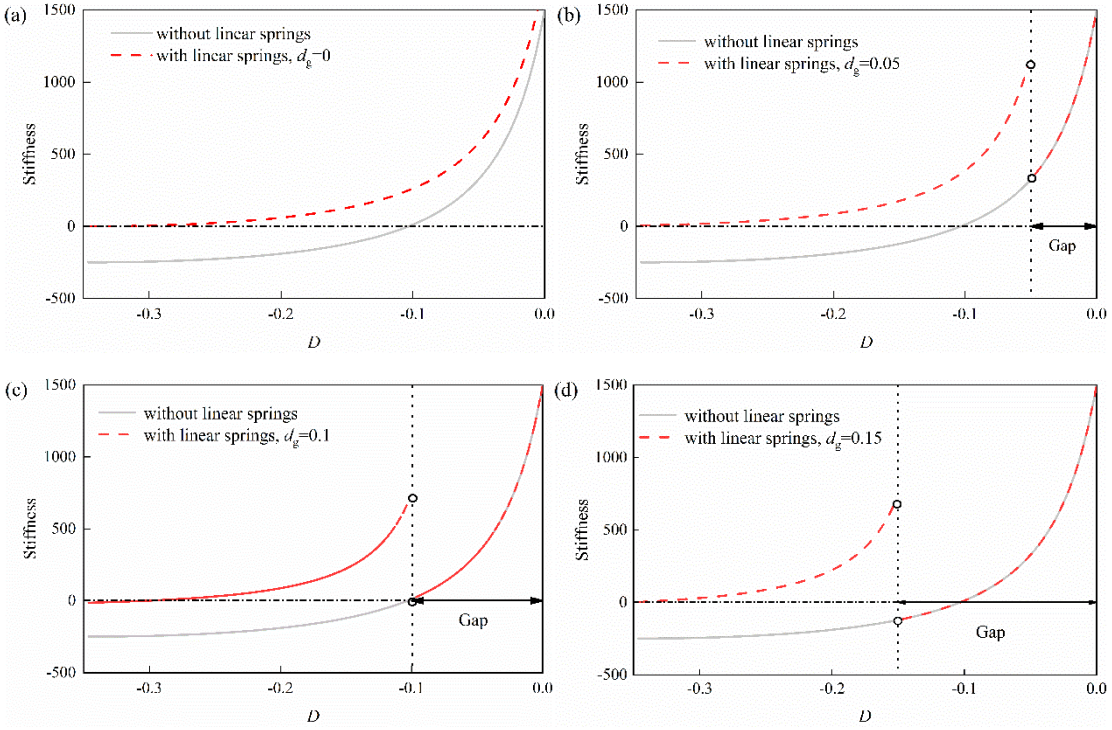

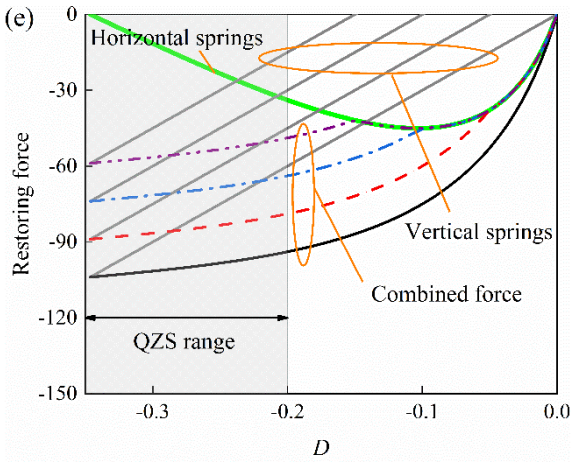

Fig. 5. Effective stiffness of the system with different gap distances: **a** d_g=0; **b** d_g=0.05; **c** d_g=0.1; **d** d_g=0.15. **e** Relation of restoring force F and displacement D with different gap distances

3. Nonlinear dynamics of the hexagon structure

3.1 Dynamic model

From the analysis above, it has known that different restoring force and stiffness characteristics are presented under different static deformation D. The dynamic behaviors are also necessary to be discussed to provide the design criteria for the realization of dynamic stabilization and vibration isolation performance of the proposed structure.

Fig. 1d shows the dynamic model under a suitable load mass M at an arbitrary position. The pre-compression D_0 and the deformation λ_0 of the horizontal spring are dependent on the mass M, which reaches a static equilibrium. The relation of D_0 and λ_0 can be inferred in Eq. (1). At this time, the configuration angle of the system is represented as φ, which can be expressed as

$$\cos\varphi = \cos\theta - \frac{\lambda_0}{2a} \tag{8}$$

The absolute displacement of the mass M and the base are represented as y and z, respectively. The relative displacement $\tilde{y}$ is defined as $y-z$. The horizontal displacement of the mass m is represented as x. The angle that the joints turn is φ_1. Due to the geometric relation between the object of x, y and z, x can be obtained as

$$x = 2a\cos\varphi - 2\sqrt{a^2 - \left(a\sin\varphi + \frac{\tilde{y}}{2}\right)^2} \tag{9}$$

The kinetic energy of proposed system can be written as

$$T = \frac{1}{2}M\dot{y}^2 + 2\times\frac{1}{2}m\left((\frac{\dot{x}}{2})^2 + \left(\frac{\dot{y}+\dot{z}}{2}\right)^2\right) \tag{10}$$

where $\dot{x} = \frac{dx}{d\bar{y}}\dot{\bar{y}}$

The potential energy of the proposed system is given by

$$V = \frac{1}{2}k_h\left(\lambda_0 + x\right)^2 + 4\times\frac{1}{2}k_v\delta_1^2 - Mgy - 2mg\left(\frac{y+z}{2}\right) \tag{11}$$

The dissipated energy Q for total damping can be given by

$$Q = 2c\dot{\varphi}_1 \tag{12}$$

where c is the damping coefficients due to the joint rotational friction.

The Lagrange principle is expressed as

$$\frac{d}{dt}\left(\frac{\partial L}{\partial \dot{y}}\right) - \frac{\partial L}{\partial y} = -D \tag{13}$$

where L is the Lagrange function expressed as $L = T - V$. Substituting Eqs. (11) and (12) into (13), the equation of motion for proposed system can be obtained as

$$\begin{aligned} &M\ddot{y} + \frac{1}{2}m\left(\ddot{y}+\ddot{z}\right) + \frac{1}{2}m\left(\frac{dx}{d\bar{y}}\right)^2\ddot{\bar{y}} + m\frac{dx}{d\bar{y}}\frac{d^2x}{d\bar{y}^2}\frac{d\bar{y}}{dy}\dot{\bar{y}}^2 + k_h\left(x+\lambda_0\right)\frac{dx}{d\bar{y}}\frac{d\bar{y}}{dy} + 4k_v\delta_1\frac{d\delta_1}{d\bar{y}}\frac{d\bar{y}}{dy} + \left(M+m\right)g \\ &= -2c\frac{d\varphi_1}{d\bar{y}}\dot{\bar{y}} \end{aligned} \tag{14}$$

For convenience, define several nonlinear functions f_1, f_2, f_3 and f_4 as

$$f_1\left(\bar{y}\right) = \left(\frac{dx}{dy}\right)^2 \tag{15}$$

$$f_2\left(\bar{y}\right) = \frac{dx}{d\bar{y}}\frac{d^2x}{d\bar{y}^2}\frac{d\bar{y}}{dy} \tag{16}$$

$$f_3\left(\bar{y}\right) = \left(x+\lambda_0\right)\frac{dx}{d\bar{y}}\frac{d\bar{y}}{dy} \tag{17}$$

$$f_4\left(\bar{y}\right) = \frac{d\varphi_1}{d\bar{y}} \tag{18}$$

Substituting Eqs. (15)-(18) into (14), then the equation of motion of the proposed system can be rewritten as

$$\left(M+\frac{1}{2}m+\frac{1}{2}mf_1(\hat{y})\right)\ddot{\hat{y}}+\frac{1}{2}mf_2(\hat{y})\dot{\hat{y}}^2+k_hf_3(\hat{y})+2k_v(\hat{y}+D_0)+2cf_4(\hat{y})\dot{\hat{y}}+(M+m)g \\ =-(M+m)\ddot{z} \tag{19}$$

where

$$f_1(\hat{y})=\frac{(2a\sin\varphi+\hat{y})^2}{4a^2-(2a\sin\varphi+\hat{y})^2} \tag{20}$$

$$f_2(\hat{y})=\frac{4a^2(2a\sin\theta+\hat{y})}{\left(4a^2\cos^2\theta-4a\sin\theta\cdot\hat{y}-\hat{y}^2\right)^2} \tag{21}$$

$$f_3(\hat{y})=\frac{(\hat{y}+2a\sin\varphi)\left(2a\cos\varphi+\lambda_0-\sqrt{4a^2\cos^2\varphi-4a\sin\varphi\cdot\hat{y}-\hat{y}^2}\right)}{\sqrt{4a^2\cos^2\varphi-4a\sin\varphi\cdot\hat{y}-\hat{y}^2}} \tag{22}$$

$$f_4(\hat{y})=\frac{1}{\sqrt{4a^2\cos^2\varphi-4a\sin\varphi\cdot\hat{y}-\hat{y}^2}} \tag{23}$$

The nonlinear functions f_1, f_2, f_3 and f_4 are all continuous at $\hat{y}=0$. Thus, these functions in Eqs. (20)-(23) can be expanded by Taylor series at zero equilibrium as

$$F_1(\hat{y})=\alpha_0+\alpha_1\hat{y}+\alpha_2\hat{y}^2+\alpha_3\hat{y}^3 \tag{24}$$

$$F_2(\hat{y})=\alpha_4+\alpha_5\hat{y}+\alpha_6\hat{y}^2+\alpha_7\hat{y}^3 \tag{25}$$

$$F_3(\hat{y})=\gamma_0+\gamma_1\hat{y}+\gamma_2\hat{y}^2+\gamma_3\hat{y}^3 \tag{26}$$

$$F_4(\hat{y})=\beta_0+\beta_1\hat{y}+\beta_2\hat{y}^2+\beta_3\hat{y}^3 \tag{27}$$

where the coefficients α_0 to α_7, γ_0 to γ_3, and β_0 to β_3 are listed in the **Appendix**. Replacing the functions f_1, f_2, f_3, and f_4 by F_1, F_2, F_3 and F_4 in Eq. (19), The dynamic equation of the system is given by

$$\left(M+\frac{1}{2}m+\frac{1}{2}mF_1(\hat{y})\right)\ddot{\hat{y}}+\frac{1}{2}mF_2(\hat{y})\dot{\hat{y}}^2+k_hF_3(\hat{y})+2k_v(\hat{y}+D_0)+2cF_4(\hat{y})\dot{\hat{y}}+(M+m)g=-(M+m)\ddot{z} \tag{28}$$

It can be observed from the dynamic equation that the proposed system has complicated nonlinear inertia, stiffness and damping due to its geometric relation. All these nonlinear effects are dependent on the structural parameters, which deserves further discussion.

3.2 Nonlinear inertia

(1) Nonlinear inertia incurred equivalent mass

The nonlinear inertia of the masses attached on the joints produces equivalent mass, which is given by $mF_1(\hat{y})$ in Eq. (28). According to the component of the function $F_1(\hat{y})$, it is known that the rod-length a and the compression angle φ are two critical parameters to determine the equivalent mass.

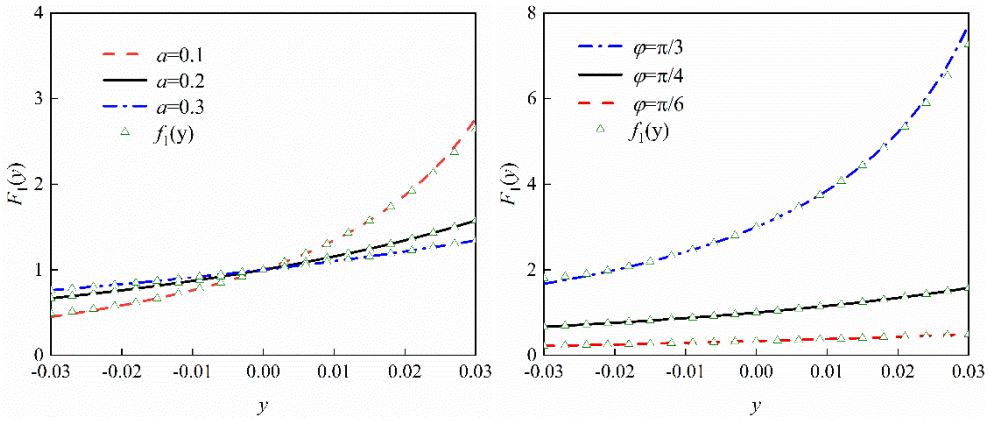

(a) (b)

Fig. 6 Function value of F_1 with different **a** length of the links a, and **b** the equilibrium positions

Fig. 6 shows the function value of $F_1(\hat{y})$ versus $\hat{y}$ with different rod-length a and the compression angle φ. It is observed that the equivalent mass constantly increases from a relative smaller value during the relative motion $\hat{y}$ changing from negative (compression) to positive (extension). This nonlinearity can lead a smaller reactive force as the smaller equivalent mass in compression. The function $F_1(\hat{y})$ changes faster with a smaller rod-length a and compression angle φ, which presents a large nonlinear. The triangle symbols represent the original function $f_1(\hat{y})$, which keeps a great consistency with the Taylor expanded function $F_1(\hat{y})$.

The equivalent mass always equals 1 when the angle $\varphi = \pi/4$, which represents the actual mass m. It is greater than 1 when the angle $\varphi = \pi/3 > \pi/4$ while less than 1 when $\varphi = \pi/6 < \pi/4$. This phenomenon can be summarized as the inertial amplification effect, which is benefit to the vibration isolation of the system. On the other hand, the masses m on the joints can be designed to much smaller than the load mass M to realize as several times smaller or larger than the original mass m, which is beneficial to the lightweight requirement.

(2) Nonlinear inertia incurred conservative force

Another nonlinear inertia term $mF_2(\hat{y})\dot{\hat{y}}^2$ in Eq. (28) is caused by the horizontal displacement of the mass m, which is dependent on the vibration displacement but also

on velocity. This term performs stronger nonlinearity than the nonlinear inertia incurred equivalent mass, as shown by the ordinate values in **Fig. 7**. The function value of $F_2(\hat{y})$ is always positive and generally increased with a small compression angle φ or a large rod length a. And it tends to be rapidly in the opposite parameters. These provide clues to clearly nonlinear effects for practical applications.

The slope of function $F_2(\hat{y})$ is similar to that of $F_1(\hat{y})$, which is always positive no matter how the structural parameters change. This leads the increase trend of the nonlinear force from compression ($\hat{y}<0$) to extension ($\hat{y}>0$). This phenomenon is beneficial to maintain the stability of mass center of the bearing platform and suppress vibration, which can be analyzed by the energy and conservative force.

The energy consumption per cycle due to the nonlinear force can be written as

$$W_e = m\int F_2(\hat{y})\dot{\hat{y}}^3 dt \tag{29}$$

Assuming the relative motion of the bearing platform $\hat{y}$ are in the form of the cosine function of time t and frequency ω. Then, the energy can be expressed as

$$\begin{aligned} W_e &= m\int(\alpha_4+\alpha_5\hat{y}+\alpha_6\hat{y}^2+\alpha_7\hat{y}^3)\dot{\hat{y}}^3 dt \\ &= -\omega^3 y_0^3 m\int_0^{\frac{2\pi}{\omega}}\left(\alpha_4+\alpha_5 y_0\cos(\omega t)+\alpha_6 y_0^2\cos^2(\omega t)+\alpha_7 y_0^3\cos^3(\omega t)\right)\sin^3(\omega t)dt = 0 \end{aligned} \tag{30}$$

where y_0 is the amplitude of the relative motion $\hat{y}$. According to Eq. (30), the energy per cycle is zero, which means the conservative force $mF_2(\hat{y})\dot{\hat{y}}^2$ does not dissipate or output energy.

The whole cycle can be divided into two processes of compression and extension, which result in the releasing and absorbing of the energy. For example, the energy incurred by the force during the compression period is given by

$$\begin{aligned} W_u &= -\omega^3 y_0^3 m\int_{\frac{\pi}{\omega}}^{\frac{2\pi}{\omega}}\left(\alpha_4+\alpha_5 y_0\cos(\omega t)+\alpha_6 y_0^2\cos^2(\omega t)+\alpha_7 y_0^3\cos^3(\omega t)\right)\sin^3(\omega t)dt \\ &= \omega^3 y_0^3 m\left(\frac{4}{3}\alpha_4+\frac{4}{15}\alpha_6 y_0^3\right) \end{aligned} \tag{31}$$

The relative motion $\hat{y}$ moves from -y_0 to y_0 and time t is from π/ω to $2\pi/\omega$ during the compression. The positive value in Eq. (31) means that the energy is absorbed in the compression period, which is helpful for suppressing the vibration amplitude with energy absorbed. On the contrary, the energy is negative and released in the extension period. This phenomenon can maintain stability of the platform.

The conservative force $mF_2(\hat{y})\dot{\hat{y}}^2$ can be expressed in another form. Firstly, the

velocity in one cycle can be written as

$$\dot{\hat{y}} = -\omega y_0 \sin(\omega t) = \begin{cases} -\omega\sqrt{y_0^2 - \hat{y}^2} & t \in [0, \frac{\pi}{\omega}] \\ \omega\sqrt{y_0^2 - \hat{y}^2} & t \in [\frac{\pi}{\omega}, \frac{2\pi}{\omega}] \end{cases} \tag{32}$$

Based on that, the conservative force F_c can be given by

$$F_c = mF_2(\hat{y})\dot{\hat{y}}^2 = \omega^2 mF_2(\hat{y})(y_0^2 - \hat{y}^2) \tag{33}$$

It is observed that the conservative force F_c depends on the nonlinear function $F_2(\hat{y})$. Then, it can be inferred that the conservative force F_c provides bigger force for platform extension based on the slope of $F_2(\hat{y})$ in **Fig. 7**. This can compensate for insufficient spring support force for platform extension and reduce the vertical motions of the structure.

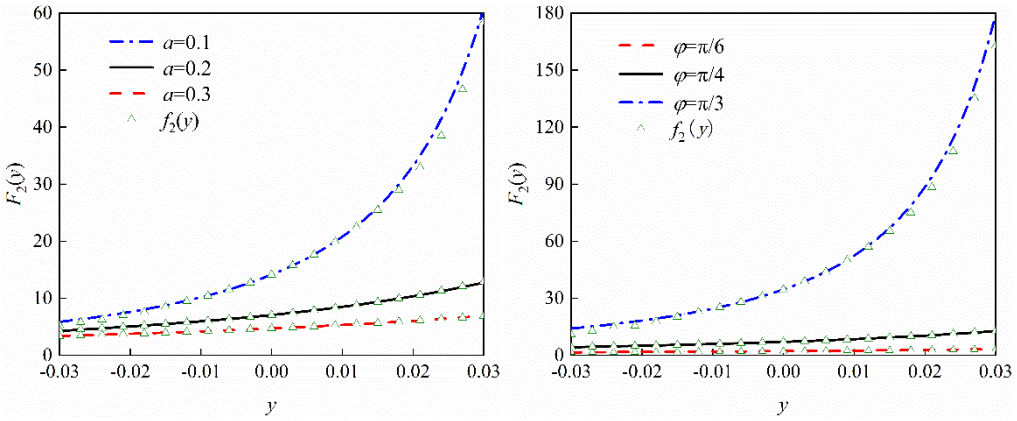

(a) (b)

Fig. 7 Function value of F_2 with different **a** length of the links a, and **b** the equilibrium position

3.3 Nonlinear stiffness

The nonlinear stiffness term $k_h F_3(\hat{y})$ of the system is given by the deformation of the horizontal spring. According to the Eq. (28), the function $F_3(\hat{y})$ is related to the initial angle θ, the compressed angle φ and the rod length a. Two angles represent the location and level of the compression.

Fig. 8a shows the bearing platform are compressed to same position at $\varphi=\pi/6$ from different initial angle θ. It is observed that the nonlinear stiffness term is always negative, which can be optimized with linear vertical springs to realize the QZS characteristic. The slope of the function $F_3(\hat{y})$ is flat with a large initial angle θ, and tends to be gradient as θ decreases. The value of $F_3(\hat{y})$ also become large with a small initial angle.

Fig. 8b shows the value of nonlinear stiffness versus variable $\tilde{y}$ at different configuration angles with the compressed angle θ-φ same. It is inferred that the value of nonlinear stiffness is small and changes slowly with a small initial angle (deeper concave). And it behaves stronger nonlinearity when the angle θ closing to $\pi/2$. The stiffness coefficient becomes larger as the rod length a increases, as shown in **Fig. 8**c.

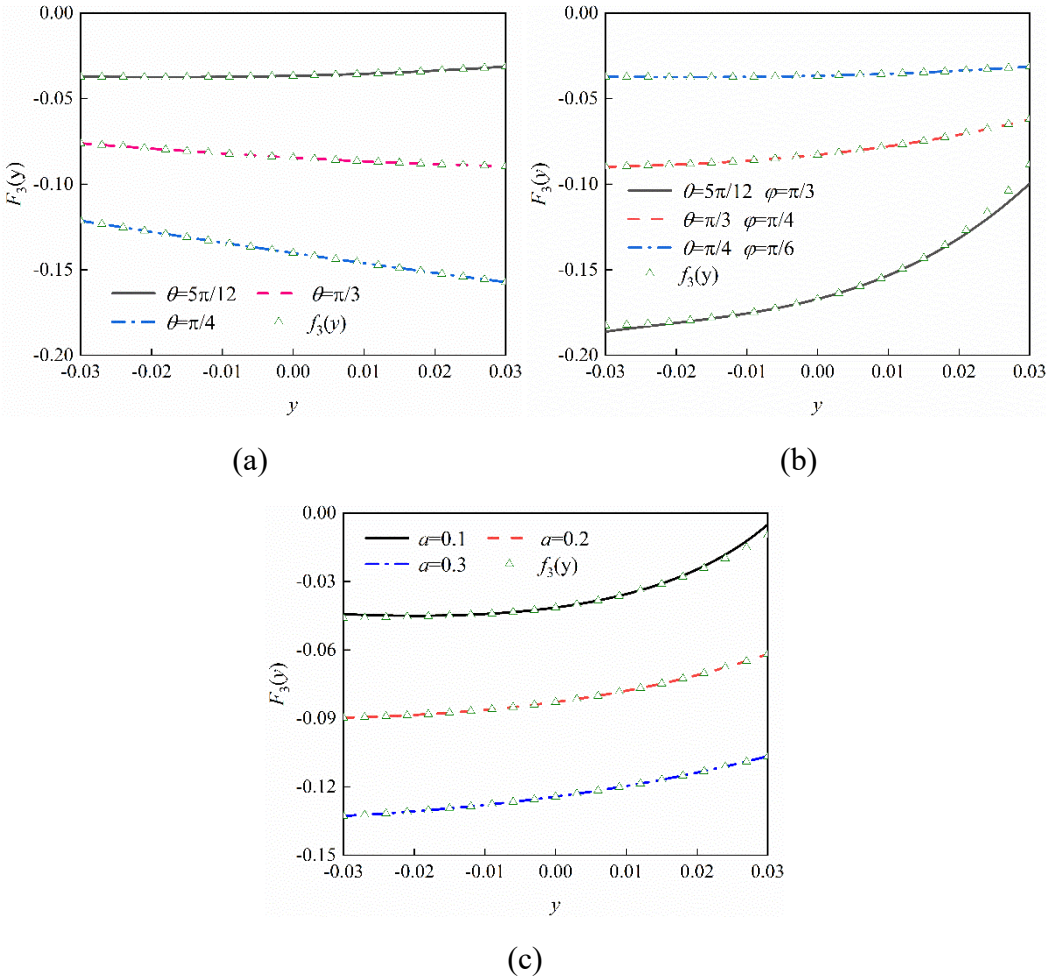

Fig. 8 Function value of $F_3(y)$ with different **a** compression range, **b** configuration angle and **c** rod length

According to the Taylor expand function $F_3(y)$, the expression of the effective stiffness at the equilibrium of the system can be simplified as

$$k_{eff} = k_h \gamma_0 + 2k_v D_0 \tag{34}$$

To realize the QZS characteristic, Eq. (34) can be expressed as

$$\left(\frac{\cos\theta}{\cos\varphi^3} - 1 \right) + 2\kappa = 0 \tag{35}$$

where $\kappa = k_v / k_h$ is the stiffness ratio. The structural parameters κ, θ, and φ need to

meet the requirement in Eq. (35) to make the effective stiffness zero. When the initial angle $\theta = \pi/2$ and the stiffness ratio $\kappa = 0.5$, the system has a zero effective stiffness for a full compression range, which is consistent with the results in **Section** 2.2.

Fig. 9a shows the relation among three parameters when they meet Eq. (35), which provides a reference for the design and optimization of the structure for vibration isolation. The stiffness ratio κ increases from 0 to 0.5 with the initial angle θ increasing to $\pi/2$ under a certain compression angle φ. The larger the initial angle θ is, the wider the compression range is at the expense of changing the stiffness ratio to obtain a zero stiffness.

However, the zero stiffness only can be realized at a certain point, which is not suitable for practical engineering applications with variable load. Therefore, it has great significance to explore the QZS range around the zero-stiffness position, which also has great vibration isolation effect. Three points with $\kappa = 0.1$, 0.2 and 0.3 in **Fig. 9**a are selected to explore the QZS range. Here, the difference between QZS and zero-stiffness can be defined as the ratio of the effective stiffness and the linear vertical stiffness of the systems, called κ_e. Different colored areas represent the range of κ_e in **Fig. 9**b. When $\theta = \pi/4$ and $\kappa = 0.1$, the platform is allowed to compressed in a narrow range with the limit that the QZS range κ_e is less than 0.01. Once the constraint of the QZS range is relaxed to 0.02 or 0.05, the corresponding range becomes wider. When the initial angle θ becomes large, the allowed compression range has an obvious improvement, which is a more effective means to widen the working range. These indicate clearly QZS characteristics and an optimization is needed for specific practical applications.

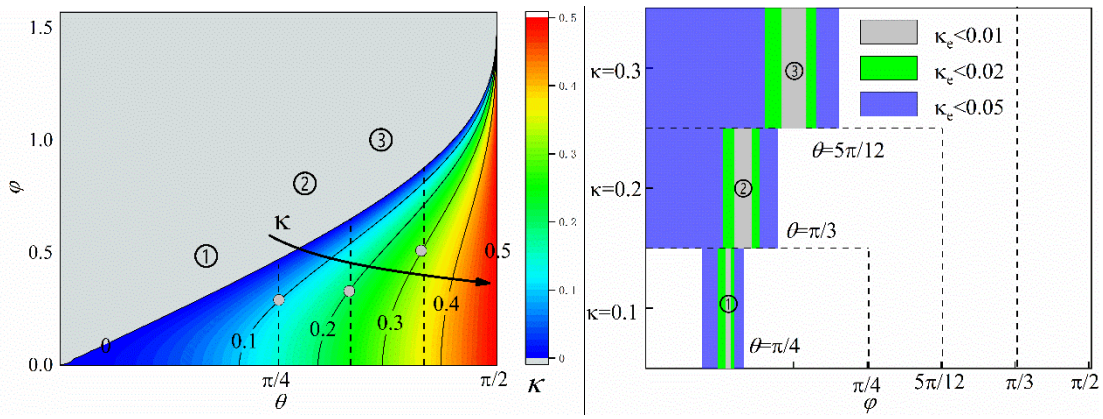

(a) (b)

Fig. 9 a Relation among three structural parameters at the zero-stiffness point. **b**

Compression ranges of the platform with different initial angles and QZS ranges

3.4 Nonlinear damping

Damping coefficient has obvious influence on the amplitude of vibration. It can absorb vibration energy from the system. The damper consists of the linear and nonlinear damping property given by the vertical motion y and the rotation of the joints φ, respectively. The latter is determined by the coefficient $2cF_4(\hat{y})$ in Eq. (29).

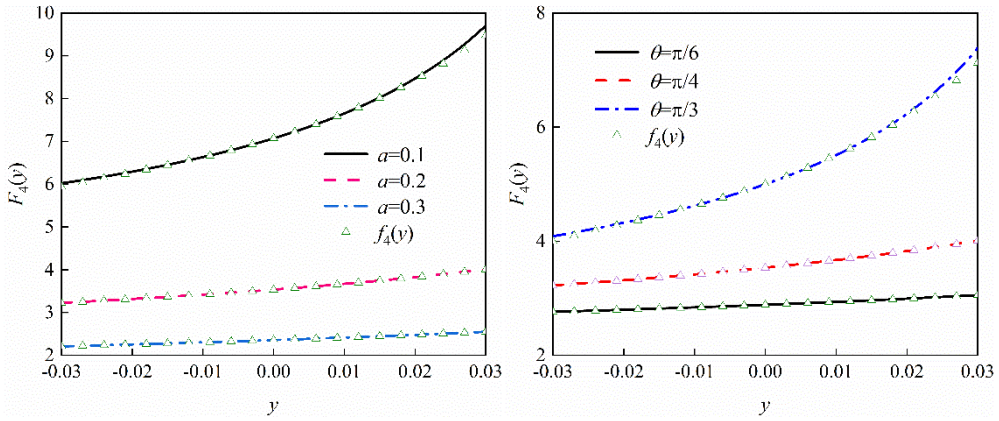

(a) (b)

Fig. 10 Nonlinear damping coefficient $F_4(\hat{y})$ versus $\hat{y}$ with different **a** original angle θ and **b** rod length a

Fig. 10 shows the nonlinear damping function $F_4(\hat{y})$ versus $\hat{y}$ with different initial angle θ and rod length a. The damping coefficient tends to be a constant small value for big rod length and small initial angle, and behaves a large nonlinear on the contrary. It is also asymmetrical with respect to the vibration displacement $\hat{y}$, which tends to be much large for $\hat{y}>0$ in extension. This provides the excellent vibration isolation performance for high frequency while reducing the low frequency vibration, which is similar to the result in the **work** [33].

The dissipated energy per cycle caused by the nonlinear damping force can be written as

$$W_{\mathrm{d}} = 2c\int F_4(\hat{y})\dot{\hat{y}}^2 dt \tag{36}$$

Substituting the relative terms in **Appendix** into Eq. **(36)**, the dissipated energy can be expressed as

$$\begin{aligned} W_d &= c\omega^2 y_0^2 \int_0^{\frac{2\pi}{\omega}} \left(\beta_0 + \beta_1 y_0 \cos(\omega t) + \beta_2 y_0^2 \cos^2(\omega t) + \beta_3 y_0^3 \cos^3(\omega t)\right)\sin^2(\omega t) dt \\ &= c\omega^2 y_0^2 \left(\beta_0 + \frac{1}{4}\beta_2 y_0^2\right) \end{aligned} \tag{37}$$

The dissipated energy is determined by the nonlinear terms β_0 and β_2, which is related to the structural parameters *a* and θ. Hence, the energy dissipation in vibration system can be adjusted to optimize the isolation performance.

4. Vibration isolation performance

4.1 Displacement transmissibility

To evaluate the vibration isolation performance of the proposed QZS structure, the displacement transmissibility is obtained under the harmonic excitations. Substituting the Taylor series expansion in Eqs. (24) to (27) into Eq. (29), the complete equation of motion can be rewritten as

$$\begin{aligned}&\left(M+\frac{1}{2}m+\frac{1}{2}m(\alpha_0+\alpha_1 y+\alpha_2 y^2+\alpha_3 y^3)\right)\ddot{y}+\frac{1}{2}m(\alpha_4+\alpha_5 y+\alpha_6 y^2+\alpha_7 y^3)\dot{y}^2+k_h(\gamma_0+\gamma_1 y+\gamma_2 y^2+\gamma_3 y^3)\\&+2k_v(\hat{y}+D_0)+2c(\beta_0+\beta_1 y+\beta_2 y^2+\beta_3 y^3)\dot{y}+(M+m)g=-(M+m)\ddot{z}\end{aligned} \tag{38}$$

where the base excitation $z=z_0\cos(\omega t+\phi)$. The solution of the displacement response in Eq. (38) can be set as $\hat{y}=y_0\cos\omega t$. Then, the phase ϕ can be derived with the harmonic balance mothed and neglecting higher-order harmonics, as

$$\begin{cases}\cos\phi=\dfrac{\left(4k_v+2k_h\left(\gamma_1+\dfrac{3}{4}{y_0}^2\gamma_3\right)-\left(2M+m\left(1+\alpha_0+\dfrac{1}{4}{y_0}^2\left(3\alpha_2-2\alpha_5-\alpha_5{y_0}^2\right)\right)\right)\omega^2\right){y_0}^2}{(2M+m)\omega^2 z_0}\\ \sin\phi=-\dfrac{\left(4\beta_0+\beta_2 y_0^2\right)c\omega y_0^2}{(2M+m)\omega^2 z_0}\end{cases} \tag{39}$$

According to the trigonometry operations $\cos^2\phi+\sin^2\phi=1$, the relation of the amplitude and frequency can be solved in Eq. (39). Then, the displacement transmissibility T_d can be derived as

$$T_d=20\lg\left(\frac{\sqrt{y_0^2+z_0^2+2y_0z_0\cos\phi}}{z_0}\right) \tag{40}$$

For different stiffness distributions of k_h and k_v, the structure has different load capacity and stiffness characteristics. As the vertical stiffness k_v increases from 50 N/m to 200 N/m for k_h=500 N/m in **Fig. 11**, the load capacity of the system increases and the effective stiffness gradually changes from negative to quasi-zero, then to positive. When the horizontal stiffness k_v=0, the structure becomes a linear system. Both points B and E in **Fig. 11**b exhibit QZS characteristics, though the load capacity and the degrees of the nonlinearity around the equilibrium position are different. Therefore, the amplitude-frequency response for different structural configuration cannot be generalized.

Fig. 11c shows the transmissibility curves of five points A~E in **Fig. 11**a and b with the initial angle $\theta=\pi/3$ and damping $c=0.5$. Point A has a good performance on transmissibility curves with a negative stiffness, though the unstable case is not suitable for this work. Points B C and E have an obvious frequency jump. The starting frequency of the jump for point C is much larger than points B and E, because B and E behave positive and quasi-zero stiffness, respectively. The peak of the transmissibility curve for point C occurs around the resonant frequency $\omega_0 \approx \sqrt{k_e/M} = 3.40$. The jump-down phenomenon of the transmissibility curve for point E is more evident than that of point B. It can be explained by the strong nonlinearity of the stiffness for point E and the large damp effect for point B under a large compression, as discussed in **Fig. 10**b. The transmissibility curve of point D has no frequency jump because of the linear system, and the peak of the curve also occurs around the resonant frequency $\omega_0 \approx \sqrt{2k_v/M} = 5.98$. In the above analysis, it can be observed that the QZS characteristics bring greater vibration isolator performance than the positive stiffness and linear systems, especially the case with weaken nonlinearity of QZS characteristic around the equilibrium position.

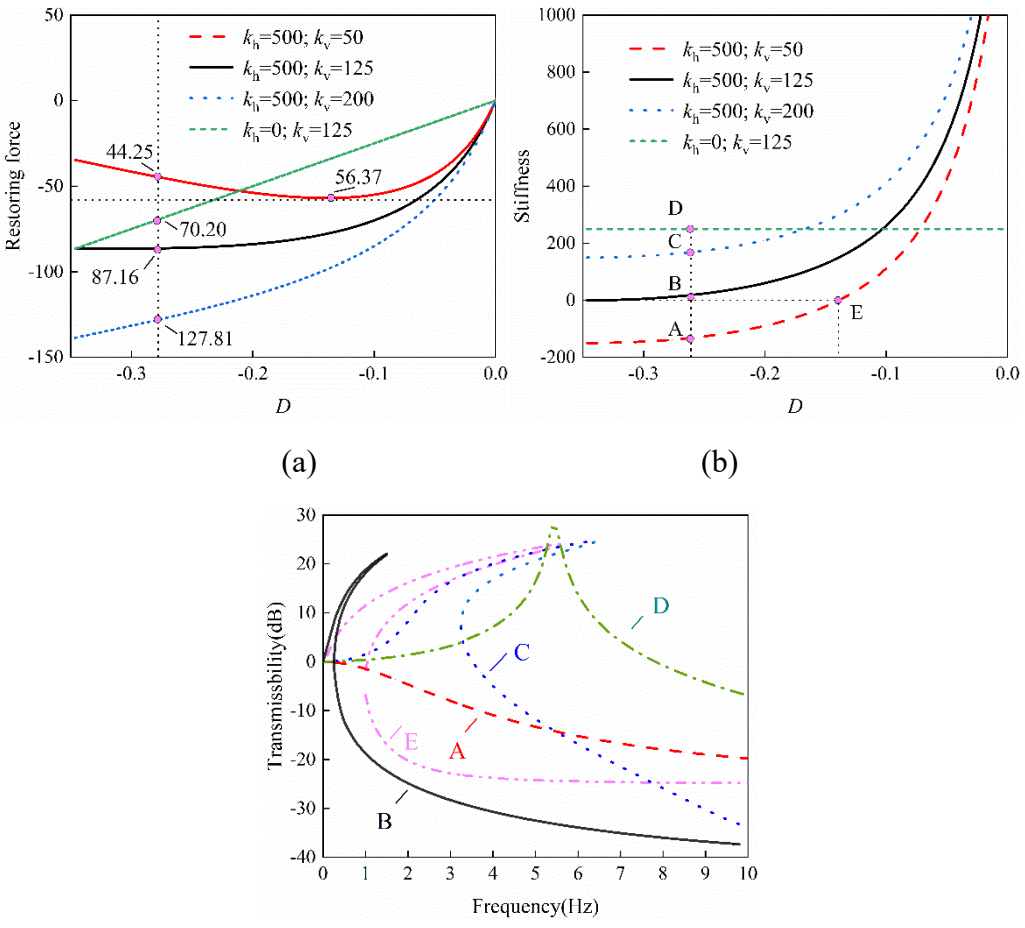

Fig. 11 a Load capacity, **b** effective stiffness and **c** transmissibility of five typical stiffness

distributions

4.2 Parametric influence of the transmissibility

The displacement transmissibility is influenced complicatedly by several parameters including angles θ, φ, damping c, and base excitation z_0. Although it is difficult to obtain a specific expression, the general rules of the parametric influence can be conducted to demonstrate the sensitivity of the displacement transmissibility to θ, φ, c, z_0, m and a. as shown in **Fig. 12**.

The effect of the initial angle θ on the hexagon QZS vibration isolator is shown in **Fig. 12**a and b. The load capacity of the platform is set to be the same for better comparison of the effect of different angles, which is realized by adjusting the compression distance D_0, as shown in **Fig. 12**a. Based on that, the displacement transmissibility solved in **Fig. 12**b. The result indicates that the vibration isolation performance becomes better as the initial angle θ decreases from π/3 to π/6 under the same load. The frequency jump phenomenon is more obvious with a large angle θ. It can be explained that a small effective stiffness is easier to achieve by using a small initial angle for the same load, which is good for low frequency vibration isolation. According to the stiffness characteristics, the platform can have a good isolation performance for a large initial angle when a heavier load is applied, which cannot be realized by a small initial angle. As mentioned in **Section 2.2**, the structure has a zero stiffness for the whole compression range when the initial angle $\theta=\pi/2$. It is hard to solve the displacement transmissibility due to the stiffness term is completely zero. However, an experiment with another similar zero stiffness structure has been used to verify the vibration isolation performance [38].

The effect of the compression angle φ on the hexagon QZS vibration isolator is shown in **Fig. 12**c and d. The load capacity increases as the compression angle φ changing from π/4 to π/6 under a same initial angle $\theta=\pi/3$, as shown in **Fig. 12**c. The resonant frequency of the transmissibility curve increases under less compression, which indicates that the vibration isolation performance is better by using a small compression angle.

The effect of the damping c of the structure is shown in **Fig. 12**e. The other structural parameters are set as the same with that of point B in **Fig. 11**. It is observed that the frequency responding to the peak of the transmissibility curves remains unchanged with different damping. But the jump frequency becomes lower and the nonlinearity is weaker as the damping increases from 0.3 to 0.7, the peak values of the transmissibility also become smaller.

The effect of the amplitude of the base excitation z_0 of the structure is shown in

Fig. 12f. For the proposed QZS structure, its transmissibility is significantly affected by the excitation amplitude. When the amplitude z_0 increasing from 0.01 to 0.03mm, it becomes more serious for the nonlinear hardening of the system, which makes the effective isolation interval of the QZS narrowed. It indicates that the proposed QZS platform is more suitable for small excitations for the application in low-frequency isolation. However, the displacement transmissibility at high frequency does not show an obvious change with the increasing of the base excitation amplitude.

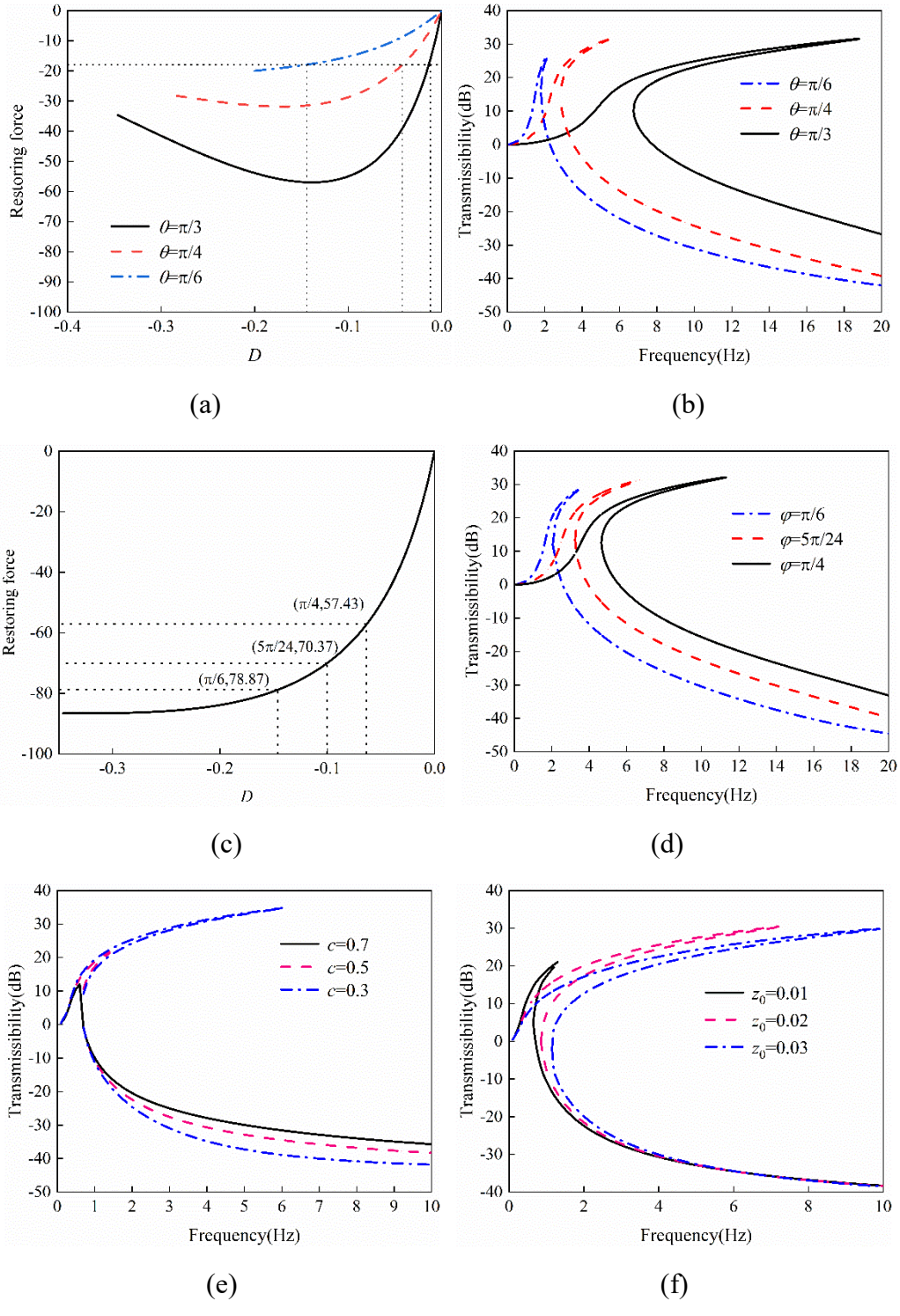

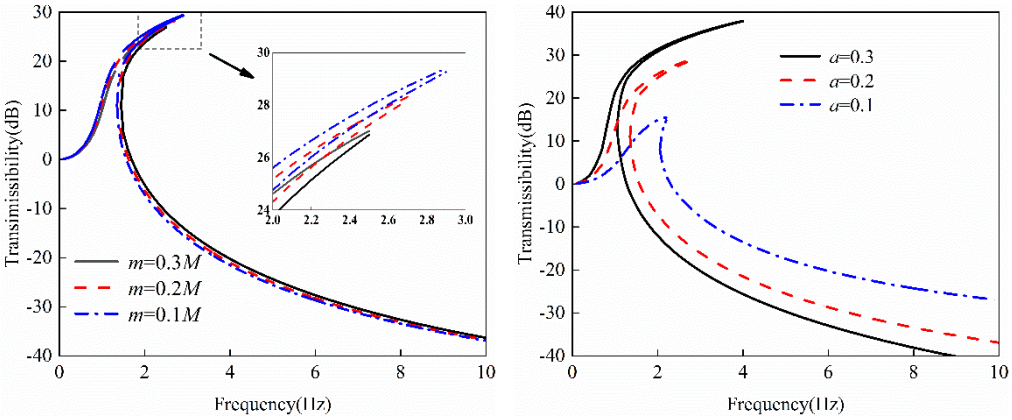

(g) (h)

Fig. 12 Displacement transmissibility curves of the proposed QZS structure with different parameters

The effect of different mass m is shown in **Fig. 12**g. Although the difference of the transmissibility curves is subtle, it can be observed that the bigger the mass m, the lower the peak of the curve. According to the static analysis in **Section 2.2**, the load capacity of the system is determined by the structural parameters. Therefore, lower displacement transmissibility is achieved with large m without influence on the payload mass M.

The effect of different rod length a is shown in **Fig. 12**h. The resonant frequency increases as the rod length decreasing from 0.3 to 0.1, which may be caused by the smaller negative stiffness coefficient with a smaller rod length a in discussion of **Section 3.3**. The peak of the transmissibility curve is lower under a smaller rod length a, which can be explained by larger damping coefficient of the system using a shorter rod.

In a summary, the transmissibility of the proposed QZS structure is determined by several parameters: angles θ, φ, damping c, base excitation z_0, mass m and rod length a. The parametric influence can be summarized as: 1) A lower resonant frequency can be obtained under a large θ with small φ, or a small θ with large φ, a large m, z_0, and a. 2) A more obvious frequency jump phenomenon can be obtained under a small θ, c and a large φ, a, z_0.

4.3 Performance comparison

To demonstrate the beneficial vibration performance of the hexagon QZS platform, the comparisons are conducted between the classical QZS system and the proposed QZS system, which both consist of three springs, as shown in **Fig. 13**a. For comparison, the stiffness of the oblique springs in classical QZS system and the vertical springs in the proposed system are set as 125 N/m, the stiffness of the remaining one is set as 500 N/m in two systems. It can be observed that the effective stiffness of the classical QZS

system is much lower than that of the linear springs, especially around the equilibrium position. However, the stiffness of the QZS increases rapidly with the increasing of the displacement, which results an obvious frequency jump phenomenon and is detrimental to attainment of large-amplitude responses in the ultralow frequency region. In the opposite, the proposed structure has a large low-stiffness region, the corresponding resonant frequency and the transmissibility of the proposed system is much lower than that of the classical QZS system, as shown in **Fig. 13**b. The effective vibration isolation frequency at 1Hz can be as low as 1/4 of that in classical one at 4Hz. When the vibration frequency is 2 Hz, the vibration is effectively isolated by the proposed structure in **Fig. 13**c, while it is still in resonance in the classical QZS isolator. Therefore, the proposed system has a better vibration isolation performance than the three-springs QZS system.

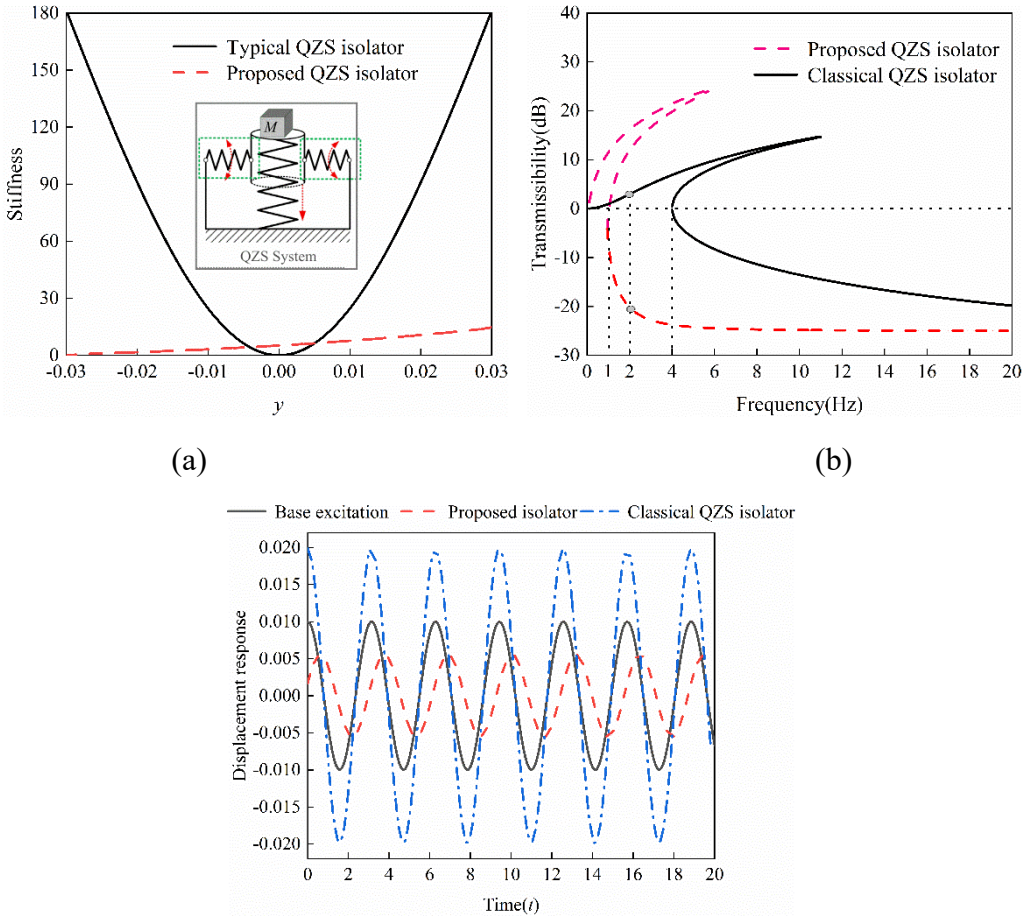

Fig. 13 a Stiffness, and **b** transmissibility characteristics for both the classical QZS system and the proposed QZS system. **c** Displacement response of two QZS isolators under 2 Hz

5. Conclusion

In this paper, a symmetric hexagon structure composed of links and springs is proposed to form a quasi-zero-stiffness platform for low-frequency vibration isolation.

The QZS stiffness characteristics for different load capacity can be realized by adjusting the structural parameters. An analytical expression for the effective stiffness is derived to achieve the QZS characteristic. Based on the analysis, a limit case when the initial angle is π/2 is explored, which has absolute zero-stiffness and can be used as a vibration isolator for the full frequency band. Then, the nonlinear inertia, nonlinear stiffness and nonlinear damping are analyzed under the dynamic response, which are all adjustable via structural parameters. The results show that they are beneficial for the structural stability and vibration suppression. The dynamic model of the structure is established based on the Lagrange equation and the displacement transmissibility is solved by the harmonic balance method to predicting its vibration isolation performance. The results show that the proposed structure can realize effective suppression of the vibration at a lower starting frequency under the QZS characteristic. The resonant frequency can be reduced comparing to the linear structure even if the effective stiffness increases due to the load changes. In addition, the occurrence of the frequency jump phenomenon can be adjusted by structural parameters for the long-term stable work of the platform. Comparing with classical QZS isolator, it has a wider quasi-zero stiffness plateau and lower starting frequency of the transmissibility. The effective vibration isolation frequency can be as low as 1/4 of that in classical one. This work provides a potential approach to passive vibration isolation in low even full frequency band.

Acknowledgements

This work was supported by the National Natural Science Foundation of China (12172383), and the Project of State Key Laboratory of High Performance Complex Manufacturing (ZZYJKT2020).

Data Availability

The datasets generated during and/or analyzed during the current study are available from the corresponding author on reasonable request.

Compliance with ethical standards

Conflict of interest

No conflicts of interest by submitting this paper.

Appendix

$$\alpha_0 = \tan^2\varphi,\quad \alpha_1 = \frac{\sin\varphi}{a\cos^4\varphi},\quad \alpha_2 = \frac{5-3\cos 2\varphi}{8a^2\cos^6\varphi},\quad \alpha_3 = \frac{3\left(3-\cos 2\varphi\right)\sin\varphi}{12a^3\cos^8\varphi};$$

$$\alpha_4 = \frac{\sin\theta}{2a\cos^4\theta},\quad \alpha_5 = \frac{5-3\cos 2\theta}{8a^2\cos^6\theta},\quad \alpha_6 = \frac{3\sin\theta\left(3-\cos 2\theta\right)}{8a^3\cos^8\theta},\quad \alpha_7 = \frac{3\left(6+5\left(2\sin^4\theta-\cos^4\theta\right)\right)}{24a^4\cos^{10}\theta};$$

$\gamma_0 = \lambda_0 \tan\varphi$, $\gamma_1 = \frac{\lambda_0}{2a\cos^3\varphi} + \tan^2\varphi$, $\gamma_2 = \frac{3(\lambda_0 + 2a\cos\varphi)\tan\varphi}{8a^2\cos^4\varphi}$,

$\gamma_3 = \frac{(\lambda_0 + 2a\cos\varphi)(3 - 2\cos 2\varphi)}{16a^3\cos^7\varphi}$;

$\beta_0 = \frac{1}{2a\cos\theta}$, $\beta_1 = \frac{\sin\theta}{4a^2\cos^3\theta}$, $\beta_2 = \frac{(2 - \cos 2\theta)}{16a^3\cos^5\theta}$, $\beta_3 = \frac{3(4 - \cos 2\theta)\sin\theta}{96a^4\cos^7\theta}$;

Reference

1. Mao, X.Y., Ding, H., Chen, L.Q.: Vibration of Flexible Structures under Nonlinear Boundary Conditions. J. Appl. Mech. Trans. ASME. 84, 1–11 (2017). https://doi.org/10.1115/1.4037883
2. Li, L., Tan, L., Kong, L., Wang, D., Yang, H.: The influence of flywheel micro vibration on space camera and vibration suppression. Mech. Syst. Signal Process. 100, 360–370 (2018). https://doi.org/10.1016/j.ymssp.2017.07.029
3. Robertson, W.S., Kidner, M.R.F., Cazzolato, B.S., Zander, A.C.: Theoretical design parameters for a quasi-zero stiffness magnetic spring for vibration isolation. J. Sound Vib. 326, 88–103 (2009). https://doi.org/10.1016/j.jsv.2009.04.015
4. Liu, C., Jing, X., Daley, S., Li, F.: Recent advances in micro-vibration isolation. Mech. Syst. Signal Process. 56–57, 55–80 (2015). https://doi.org/10.1016/j.ymssp.2014.10.007
5. Zhang, J.Z., Li, D., Chen, M.J., Dong, S.: An Ultra-Low Frequency Parallel Connection Nonlinear Isolator for Precision Instruments. Key Eng. Mater. 257–258, 231–236 (2004). https://doi.org/10.4028/www.scientific.net/kem.257-258.231
6. Zhou, J., Wang, X., Xu, D., Bishop, S.: Nonlinear dynamic characteristics of a quasi-zero stiffness vibration isolator with cam-roller-spring mechanisms, (2015)
7. Xiuting, S., Zhang, S., Xu, J., Wang, F.: Dynamical Analysis and Realization of an Adaptive Isolator. J. Appl. Mech. Trans. ASME. 85, 1–13 (2018). https://doi.org/10.1115/1.4038285
8. Wu, W., Chen, X., Shan, Y.: Analysis and experiment of a vibration isolator using a novel magnetic spring with negative stiffness. J. Sound Vib. 333, 2958–2970 (2014). https://doi.org/10.1016/j.jsv.2014.02.009
9. Lu, Z., Tiejun, Y., Brennan, M.J., Liu, Z., Chen, L.Q.: Experimental Investigation of a Two-Stage Nonlinear Vibration Isolation System with High- Static-Low-Dynamic Stiffness. J. Appl. Mech. Trans. ASME. 84, 1–9 (2017). https://doi.org/10.1115/1.4034989
10. Carrella, A., Brennan, M.J., Kovacic, I., Waters, T.P.: On the force transmissibility of a vibration isolator with quasi-zero-stiffness. J. Sound Vib. 322, 707–717 (2009). https://doi.org/10.1016/j.jsv.2008.11.034
11. Kim, K.R., You, Y. han, Ahn, H.J.: Optimal design of a QZS isolator using flexures for a wide range of payload. Int. J. Precis. Eng. Manuf. 14, 911–917 (2013). https://doi.org/10.1007/s12541-013-0120-0
12. Ding, H., Ji, J., Chen, L.Q.: Nonlinear vibration isolation for fluid-conveying pipes using quasi-zero stiffness characteristics. Mech. Syst. Signal Process. 121, 675–

688 (2019). https://doi.org/10.1016/j.ymssp.2018.11.057
13. Zang, J., Zhang, Y.W., Ding, H., Yang, T.Z., Chen, L.Q.: The evaluation of a nonlinear energy sink absorber based on the transmissibility. Mech. Syst. Signal Process. 125, 99–122 (2019). https://doi.org/10.1016/j.ymssp.2018.05.061
14. Ribeiro, P., Amabili, M.: Special issue on Geometrically non-linear vibrations of structures-euromech 483. J. Sound Vib. 315, 371–374 (2008). https://doi.org/10.1016/j.jsv.2008.04.017
15. Carrella, A., Brennan, M.J., Waters, T.P.: Static analysis of a passive vibration isolator with quasi-zero-stiffness characteristic. J. Sound Vib. 301, 678–689 (2007). https://doi.org/10.1016/j.jsv.2006.10.011
16. Zhang, H., Gao, R., Zhang, J., Gao, J.: Static characteristic and vibration dynamic response analysis of switched reluctance motor system. 2009 IEEE Int. Conf. Mechatronics Autom. ICMA 2009. 557–561 (2009). https://doi.org/10.1109/ICMA.2009.5246705
17. Liu, X., Huang, X., Hua, H.: On the characteristics of a quasi-zero stiffness isolator using Euler buckled beam as negative stiffness corrector. J. Sound Vib. 332, 3359–3376 (2013). https://doi.org/10.1016/j.jsv.2012.10.037
18. Wang, K., Zhou, J., Xu, D.: Sensitivity analysis of parametric errors on the performance of a torsion quasi-zero-stiffness vibration isolator. Int. J. Mech. Sci. 134, 336–346 (2017). https://doi.org/10.1016/j.ijmecsci.2017.10.026
19. Zhou, J., Xu, D., Bishop, S.: A torsion quasi-zero stiffness vibration isolator. J. Sound Vib. 338, 121–133 (2015). https://doi.org/10.1016/j.jsv.2014.10.027
20. Xu, D., Yu, Q., Zhou, J., Bishop, S.R.: Theoretical and experimental analyses of a nonlinear magnetic vibration isolator with quasi-zero-stiffness characteristic. J. Sound Vib. 332, 3377–3389 (2013). https://doi.org/10.1016/j.jsv.2013.01.034
21. Zhou, J., Xiao, Q., Xu, D., Ouyang, H., Li, Y.: A novel quasi-zero-stiffness strut and its applications in six-degree-of-freedom vibration isolation platform. J. Sound Vib. 394, 59–74 (2017). https://doi.org/10.1016/j.jsv.2017.01.021
22. Wang, K., Zhou, J., Cai, C., Xu, D., Xia, S., Wen, G.: Bidirectional deep-subwavelength band gap induced by negative stiffness. J. Sound Vib. 515, 116474 (2021). https://doi.org/10.1016/j.jsv.2021.116474
23. Yan, B., Ma, H., Zheng, W., Jian, B., Wang, K., Wu, C.: Nonlinear electromagnetic shunt damping for nonlinear vibration isolators. IEEE/ASME Trans. Mechatronics. 24, 1851–1860 (2020). https://doi.org/10.1109/TMECH.2019.2928583
24. Yan, B., Ma, H., Jian, B., Wang, K., Wu, C.: Nonlinear dynamics analysis of a bi-state nonlinear vibration isolator with symmetric permanent magnets. Nonlinear Dyn. 97, 2499–2519 (2019). https://doi.org/10.1007/s11071-019-05144-w
25. Pu, H., Yuan, S., Peng, Y., Meng, K., Zhao, J., Xie, R., Huang, Y., Sun, Y., Yang, Y., Xie, S., Luo, J., Chen, X.: Multi-layer electromagnetic spring with tunable negative stiffness for semi-active vibration isolation. Mech. Syst. Signal Process. 121, 942–960 (2019). https://doi.org/10.1016/j.ymssp.2018.12.028
26. Chang, Y., Zhou, J., Wang, K., Xu, D.: Theoretical and experimental investigations on semi-active quasi-zero-stiffness dynamic vibration absorber. Int.

J. Mech. Sci. 214, 106892 (2022). https://doi.org/10.1016/j.ijmecsci.2021.106892
27. Feng, X., Jing, X.: Human body inspired vibration isolation: Beneficial nonlinear stiffness, nonlinear damping & nonlinear inertia. Mech. Syst. Signal Process. 117, 786–812 (2019). https://doi.org/10.1016/j.ymssp.2018.08.040
28. Feng, X., Jing, X., Xu, Z., Guo, Y.: Bio-inspired anti-vibration with nonlinear inertia coupling. Mech. Syst. Signal Process. 124, 562–595 (2019). https://doi.org/10.1016/j.ymssp.2019.02.001
29. Gatti, G.: A K-shaped spring configuration to boost elastic potential energy. Smart Mater. Struct. 28, (2019). https://doi.org/10.1088/1361-665X/ab1ec8
30. Zhao, F., Ji, J., Luo, Q., Cao, S., Chen, L., Du, W.: An improved quasi-zero stiffness isolator with two pairs of oblique springs to increase isolation frequency band. Nonlinear Dyn. 104, 349–365 (2021). https://doi.org/10.1007/s11071-021-06296-4
31. Zhang, Q., Xia, S., Xu, D., Peng, Z.: A torsion–translational vibration isolator with quasi-zero stiffness. Nonlinear Dyn. 99, 1467–1488 (2020). https://doi.org/10.1007/s11071-019-05369-9
32. Sun, X., Jing, X.: Analysis and design of a nonlinear stiffness and damping system with a scissor-like structure. Mech. Syst. Signal Process. 66–67, 723–742 (2016). https://doi.org/10.1016/j.ymssp.2015.05.026
33. Jing, X., Zhang, L., Feng, X., Sun, B., Li, Q.: A novel bio-inspired anti-vibration structure for operating hand-held jackhammers. Mech. Syst. Signal Process. 118, 317–339 (2019). https://doi.org/10.1016/j.ymssp.2018.09.004
34. Wang, Y., Jing, X., Guo, Y.: Nonlinear analysis of a bio-inspired vertically asymmetric isolation system under different structural constraints. Nonlinear Dyn. 95, 445–464 (2018). https://doi.org/10.1007/s11071-018-4575-5
35. Bian, J., Jing, X.: Analysis and design of a novel and compact X-structured vibration isolation mount (X-Mount) with wider quasi-zero-stiffness range. Nonlinear Dyn. 101, 2195–2222 (2020). https://doi.org/10.1007/s11071-020-05878-y
36. Sun, X., Wang, F., Xu, J.: A novel dynamic stabilization and vibration isolation structure inspired by the role of avian neck. Int. J. Mech. Sci. 193, 106166 (2021). https://doi.org/10.1016/j.ijmecsci.2020.106166
37. Yan, G., Zou, H.-X., Wang, S., Zhao, L.-C., Gao, Q.-H., Tan, T., Zhang, W.-M.: Large stroke quasi-zero stiffness vibration isolator using three-link mechanism. J. Sound Vib. 478, 115344 (2020). https://doi.org/10.1016/j.jsv.2020.115344
38. Wu, L., Wang, Y., Zhai, Z., Yang, Y., Krishnaraju, D., Lu, J., Wu, F., Wang, Q., Jiang, H.: Mechanical metamaterials for full-band mechanical wave shielding. Appl. Mater. Today. 20, (2020). https://doi.org/10.1016/j.apmt.2020.100671